AMOEBA Polarizable Force Field for Molecular Dynamics Simulations of Glyme Solvents

Tobias Binninger, Defne Saraç, Liam Marsh, Tanguy Picard, Marie-Liesse Doublet, Christophe Raynaud

AMOEBA Polarizable Force Field for Molecular Dynamics Simulations of Glyme Solvents

Tobias Binninger,[†] Defne Saraç,[†,‡] Liam Marsh,[†] Tanguy Picard,[¶] Marie-Liesse Doublet,[†,‡] and Christophe Raynaud[*,†]

[†]*ICGM, Univ Montpellier, CNRS, ENSCM, Montpellier, France*

[‡]*Réseau sur le Stockage Electrochimique de l'Energie (RS2E), FR CNRS 3459, Hub de l'Energie, Amiens, France*

[¶]*Univ. Grenoble Alpes, Univ. Savoie Mont Blanc, CNRS, Grenoble INP, LEPMI, 38000 Grenoble, France*

E-mail: Christophe.Raynaud1@umontpellier.fr

Abstract

Classical molecular dynamics (MD) simulations of electrolyte systems are important to gain insight into the atom-scale properties that determine the battery-relevant performance. The recent Tinker-HP software release enables efficient and accurate MD simulations with the AMOEBA polarizable force field. In this work, we developed a procedure to construct a universal AMOEBA model for the solvent family of glymes (glycol methyl ethers), which involves a refinement scheme for valence parameters by fitting the AMOEBA-derived atomic forces to those computed at the DFT level. The refined AMOEBA model provides a good description of both local and non-local properties in terms of the spectroscopic response of glyme molecules, as well as the liquid glyme density and dielectric constant. In addition, the complexation energies of alkali and alkaline-earth metal cations with tetraglyme molecules obtained from AMOEBA calculations are in good agreement with DFT results, demonstrating the suitability of the developed AMOEBA model for an accurate simulation of glyme-based battery electrolytes. We also expect the procedure to be transferable to the development of AMOEBA models for other battery electrolyte systems.

Introduction

The electrolyte is one critical component determining the stability and safety of Li-ion and post-Li-ion batteries. Current electrolyte formulations typically consist of mixtures of carbonate-based solvents,[1] such as ethylene carbonate (EC) and dimethyl carbonate (DMC), that are flammable and suffer from decomposition at the electrode–electrolyte interface.[2] Glyme-based electrolytes can be suitable alternatives.[3,4] Glymes (glycol methyl ethers, Gn) are a series of polyether solvents of the form $H_3C-O-(CH_2-CH_2-O-)_nCH_3$ with variable chain length n. The limit of large n leads to poly(ethylene oxide) (PEO), which is the most widely used polymer solvent for solid polymer electrolytes.[1] Various lithium salts, including $LiClO_4$, $LiAsF_6$, $LiPF_6$, $LiBF_4$, LiBr, LiI, and LiTFSI (TFSI: bis(trifluoromethanesulfonyl)imide,

$[F_3C-SO_2-N-SO_2-CF_3]^-$), have been investigated in combination with glyme solvents,[3–6] but the ionic conductivity of such systems is generally lower in comparison to carbonate-based electrolytes. However, glymes have beneficial stability properties due to the absence of reactive functional groups.[7] For this reason, current battery developments towards Li-metal anodes and alternative cell chemistries such as Li–S and Li–O_2 have led to increased interest in glyme-based electrolytes.[2,8,9] Likewise, glyme- and PEO-based electrolytes have attracted attention for multivalent-ion cells, such as Mg- and Ca-ion batteries.[10–12]

Since the dielectric constant of glyme solvents is relatively low ($\epsilon_r \approx 7$–8)[13], the association/pairing of electrolyte ions is relevant for the ionic conductivity properties of such systems.[2,4,6,9,14] Glymes specifically interact with cations through the ether oxygens (EOs), making them good cation but poor anion solvents.[7] The multiple EOs provide chelating properties giving rise to rich solvation/complexation structures with a strong dependence on the cation nature, chain length, and electrolyte concentration.[15–17] Remarkably, highly concentrated equimolar mixtures of Li(TFSI)-type salts and triglyme (G3) or tetraglyme (G4) solvent form so-called solvate ionic liquids (SILs), where all glyme molecules and Li^+ cations are present in stable $[Li(Gn)]^+$ ($n = 3, 4$) cation complexes.[8,16,18–20] Recently, some of us reported a peculiar temperature dependence of the ionic conductivity of the $Ca^{2+}(TFSI^-)_2$–tetraglyme (G4) liquid electrolyte system.[21] The ionic conductivity was observed to decrease at elevated temperatures at which an increased presence of $[Ca(TFSI)]^+$ ion pairs was detected. To explain this behavior, the authors suggested an entropy-driven ion-pair association stemming from the competition between G4 molecules in a low-entropy state within the chelated $[Ca(G4)_2]^{2+}$ complexes and the higher entropy state of "free" G4 molecules that become liberated upon $[Ca(TFSI)(G4)]^+$ ion pairing.

Computational studies of glyme- and PEO-based electrolytes by classical molecular dynamics (MD) simulations provide relevant atomic-level insight into the relationship between solvation, ion-pairing, and ionic conductivity.[22] The force-field models that have previously been employed for simulating such systems can be classified as either non-polarizable[16,23–27]

or polarizable[28–34]. It has been highlighted that polarizability is required for an accurate description of the dielectric and dynamic properties of the electrolyte.[22,23,31,35] The APPLE&P model[36] is the most commonly used polarizable force field for MD simulations of such electrolytes to date, but also Drude oscillators were employed to account for polarizability.[33] The polarizable AMOEBA model (Atomic Multipole Optimized Energetics for Biomolecular Applications)[37] provides a very detailed description of electrostatic interactions by including both permanent atomic multipoles (monopole, dipole, quadrupole moments) and induced atomic dipoles resulting from atomic polarizabilities. Only few studies employed the AMOEBA model for the simulation of battery electrolyte systems so far,[38–40] but the recent release of the Tinker-HP software package[41] for efficient parallelized AMOEBA MD simulations makes this approach very attractive. We therefore aim to establish a protocol to develop and employ AMOEBA parametrizations for next-generation battery electrolytes.

In the present work, we focus on the glyme solvent family and develop a universal AMOEBA model that can be employed for glymes of different chain lengths. We implement refinement schemes for the corresponding AMOEBA parameters based on the agreement of atomic forces with *ab initio* forces computed at the level of density-functional theory (DFT). We assess the quality of the resulting models from the simulated properties of the glyme solvents, namely the liquid density, dielectric constant, and Raman and infrared spectra in comparison with experimental results. Moreover, the complexation energies of cations with glyme molecules are evaluated and compared with the results from *ab initio* calculations. The present study represents the basis for subsequent work to simulate glyme-based battery electrolytes up to the PEO-limit using the newly developed AMOEBA models.

Methods

We developed an AMOEBA model for the glyme solvent family $H_3C-O-(CH_2-CH_2-O-)_nCH_3$. With the intention to obtain a universal model suitable for any chain length n, we based

our parametrization on tetraglyme (G4, $n = 4$) as a smaller, yet representative Gn family member that provides a balance between the influence of intra-chain units vs. terminal groups. Moreover, in order to establish a model construction procedure that will be easily transferable to other battery electrolyte systems, we intend to use DFT calculation results as reference for the refinement of the AMOEBA model parameters. In particular, we avoid the use of experimental reference data, the availability of which might be strongly dependent on the system at hand.

AMOEBA polarizable force field. The functional form of the AMOEBA force field is presented in detail elsewhere[42]. The potential energy $U = U_{\text{val}} + U_{\text{vdW}} + U_{\text{elec}}$ is decomposed into intramolecular valence bonding contributions U_{val}, van der Waals (vdW) interactions U_{vdW}, and electrostatic interactions U_{elec}. For the glyme family, the relevant contributions to U_{val} consist in bond stretching, angle bending, stretch-bend coupling, and bond torsion. The vdW term consists in a buffered 14-7 function rather than the standard Lennard-Jones 12-6 form. The most distinctive feature of AMOEBA consists in the detailed electrostatic model employed. Each atom is described by a set of permanent atomic monopole (charge), dipole, and quadrupole moments. In addition, each atom has a certain isotropic polarizability yielding induced atomic dipole moments as a function of the local electrostatic field.

AMOEBA parametrization: Electrostatic part. The values of the C, H, and O atomic polarizabilities were directly taken from the AMOEBA-09 data set.[43] The permanent atomic multipoles were determined using the procedure described by Ren et al.[43] with the following steps.

1. Five different configurations of the G4 molecule, shown in Figure 1 with atomic coordinates given in the Supporting Information (SI), were structurally optimized at the *ab initio* quantum chemistry level of second-order Møller-Plesset perturbation theory (MP2) with a 6-311G(d,p) basis set using the Psi4 program.[44] Because of the significant size of the G4 molecule, we resort to the resolution of the identity (RI) approx-

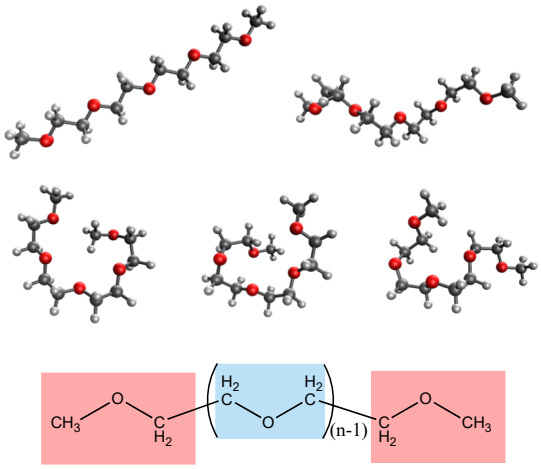

Figure 1: Structural configurations of the G4 molecule used for the distributed multipole analysis (DMA). Also shown is the decomposition of the glyme chain into charge-neutrality groups required for a universal AMOEBA parametrization for the glyme solvent family.

imation of MP2 (RI-MP2),[45] also referred to as density-fitted MP2 (DF-MP2). The DF-MP2/6-311G(d,p) densities of the optimized structures were used for a distributed multipole analysis (DMA) with the GDMA program[46] to obtain monopole, dipole and quadrupole moments of each atomic site for all five G4 configurations.

2. For each atomic site, the electrostatic monopoles obtained from the DMA of different G4 configurations were averaged. Then, we performed a "universalization" step to make the AMOEBA parametrization applicable to the entire glyme solvent family. This requires the atomic monopole charges to guarantee overall charge neutrality of the glyme molecule for any chain length, therefore implying that the charge of the $-(CH_2-O-CH_2)-$ repeating unit (blue in Figure 1) and that of the $-(CH_2-O-CH_3)$ end groups must be zero individually. To this end, we adjusted the atomic charges using an optimization scheme to minimize the squared deviation of the adjusted charges from the DMA-derived ones under the aforementioned constraints of charge neutrality for the repeating unit and end groups. Optimization was performed using SciPy[47] routines for Python. We note that the maximum change of atomic charges introduced by this universalization procedure was only 0.0026 e, and the root-mean-square deviation

(RMSD) between the initial and final set of charges was 0.001 e.

3. Finally, the DMA-derived atomic dipole and quadrupole moments were refined, while the monopole charges were kept fixed as obtained from the previous step. To this end, the electrostatic potential distribution around each of the optimized G4 configurations was determined from the electron densities obtained from DF-MP2/aug-cc-pVTZ calculations. Using the DMA-derived values as a starting point, the atomic dipole and quadrupole moments were then fitted to optimally reproduce the electrostatic potential distribution using the POTENTIAL tool of the Tinker software package.[43]

AMOEBA parametrization: Valence and vdW part. The valence parameters for bond stretching, angle bending, stretch-bend coupling, and bond torsion, as well as the vdW parameters, were taken from the AMOEBA-09 data set.[43] For each atom class of the G4 molecule, we selected a class from the available data set based on the closest matching chemical environment as follows. For the carbon and hydrogen atoms of the terminal CH_3 groups and the ether oxygen (EO) atoms, the available parameters of dimethyl ether were chosen. For the carbon and hydrogen atoms of the intra-chain CH_2 groups, the closest available match was the CH_2 group of ethanol. With this, all required valence and vdW parameters were determined with the exception of the ones for the torsional rotation of intra-chain C−O and C−C bonds involving CH_2 groups, the amplitude parameters of which were initially set to zero. In the following, this set of parameters will be referred to as *initial*.

Subsequently, we developed and tested a method to refine the valence parameters by fitting the AMOEBA-computed atomic forces to *ab initio*-computed ones. For reasons of computational cost, the latter were computed at the DFT level instead of MP2. This approach is based on the rationale that the individual atomic forces determine the motion of all species and thus the (thermo)dynamical properties of the system. A similar method has been successfully employed for the training of a deep neural network potential for MD simulations of solid-state electrolytes.[48] We thus seek to mimic, best possible, the forces obtained from

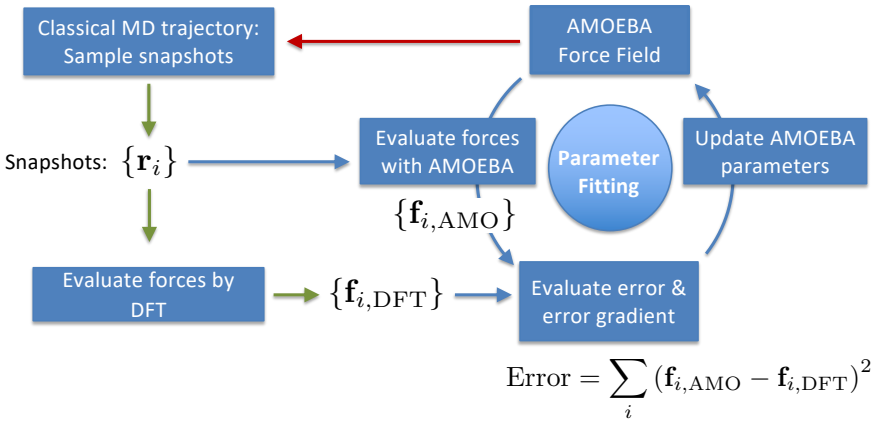

Figure 2: Refinement procedure of AMOEBA valence parameters based on the agreement of atomic forces with DFT. Forces were evaluated for snapshots that were sampled along AMOEBA MD trajectories. After convergence of the parameter fitting step, the updated AMOEBA force field was used to generate a new MD trajectory yielding a new set of snapshots. This loop of AMOEBA MD–DFT force evaluation–AMOEBA parameter fitting & update was repeated until convergence of the AMOEBA parametrization was reached.

high-level density-functional theory. To this end, the following procedure was implemented, schematically shown in Figure 2.

1. *Sampling of structural snapshots.* The MD trajectory of a single G4 molecule was computed with the Tinker software package[43] using the initial AMOEBA force field. The NVT ensemble at $T = 298.15\,\mathrm{K}$ was simulated using the Nosé-Hoover chain (NHC) thermostat and a time step of $\Delta t = 0.5\,\mathrm{fs}$. After 1 ns of thermalization, 1000 snapshots were sampled every 1 ps during another 1 ns of the trajectory. This sampling approach produces a thermodynamically meaningful set of configurations where the more stable ones are represented with a larger statistical weight than the less stable ones. Inaccuracies in the initial AMOEBA parameters are expected to produce "outlier" configurations with an enhanced deviation between AMOEBA forces and the DFT forces that will be particularly efficient for improving the AMOEBA model during the parameter fitting.

2. *Evaluating ab initio forces.* The *ab initio* reference forces were computed for the set of snapshots from the previous step. The PBE0 hybrid functional[49] and the D4 dispersion

correction[50] were used together with a triple-zeta def2-TZVP basis set. We performed these calculations using the ORCA software package.[51]

3. *Refining AMOEBA parameters.* The non-electrostatic parameters of the AMOEBA model were optimized by fitting the AMOEBA atomic forces $\mathbf{f}_{i,\mathrm{AMO}}$ to the corresponding *ab initio* forces $\mathbf{f}_{i,\mathrm{DFT}}$ computed in the previous step for the set of snapshots from the first step. The squared deviation $\sum_i \left(\mathbf{f}_{i,\mathrm{AMO}} - \mathbf{f}_{i,\mathrm{DFT}}\right)^2$ was minimized with the conjugate gradient method using SciPy[47] routines for Python, which were interfaced to the TESTGRAD tool of the Tinker software package[43] for the evaluation of the AMOEBA forces during parameter optimization. For an efficient optimization, we included a preconditioning scheme by scaling all parameters to the same order of magnitude around unity. The optimized valence parameters produced an updated AMOEBA model.

4. *Iterating the refinement procedure.* The refinement procedure was iterated by restarting the first step using the updated AMOEBA model from the third step. This refinement loop was performed three times in order to achieve self-consistency of the final AMOEBA model, which was confirmed by a negligible relative change of the parameter values by at most 0.1% during the final iteration.

The AMOEBA refinement was performed with fixed electrostatic parameters, i.e. atomic polarizabilities and multipoles. Two different refinement schemes were tested, once fitting only the valence parameters, while keeping the vdW parameters fixed at the initial values, and once fitting both valence and vdW parameters. Altogether, three different flavors of the AMOEBA model for glymes were thus obtained with (i) the initial, non-refined, (ii) the valence-refined, and (iii) the valence-vdW-refined set of parameters. The AMOEBA parametrizations developed and tested in this work are given in the SI.

Assessment of AMOEBA models. A number of relevant solvent properties were computed for the tetraglyme (G4), triglyme (G3), and diglyme (G2) members of the glyme family

by classical MD simulations with the different AMOEBA models. The starting structures of the glyme liquids were constructed using the Packmol program[52] by randomly packing 500 glyme molecules into cubic simulation cells with dimensions of $62 \times 62 \times 62\,\text{Å}^3$ for G4, $57 \times 57 \times 57\,\text{Å}^3$ for G3, and $52 \times 52 \times 52\,\text{Å}^3$ for G2. The liquid glyme cells were equilibrated by NPT MD simulations with the Tinker-HP software[41] using the velocity Verlet integrator[53] with a time step of 0.5 fs together with a Bussi-Donadio-Parrinello thermostat[54] and a Berendsen barostat,[55] which was kept at a pressure of $p = 1\,\text{atm}$. After reaching an equilibrated state, the liquid density ρ was obtained as an average over 125 ps of the NPT trajectory.

The dielectric constant ϵ_r was derived from an NVT MD simulation at $T = 298.15\,\text{K}$ using the final equilibrated cell from the corresponding NPT run as starting point. The total dipole moment $\vec{M}$ of the glyme liquid cell was extracted every 1 ps during a 2 ns trajectory, and the dielectric constant was computed from the variance of the total dipole fluctuations according to the relationship[56,57]

$$\epsilon_r = 1 + \frac{\langle \vec{M}^2 \rangle - \langle \vec{M} \rangle^2}{3\epsilon_0 k_\text{B} T V} \tag{1}$$

Whereas the density and dielectric constant are macroscopic properties of the glyme liquids, the microscopic dynamical properties are expressed in the spectroscopic response. We therefore calculated the infrared (IR) and Raman spectra from MD simulations of a single G4 molecule. The IR absorption cross section $\alpha_\text{IR}(\omega)$ is related to the Fourier transform of the autocorrelation function of the molecular dipole moment $\vec{\mu}$, or its time derivative $\dot{\vec{\mu}}$, by[58]

$$\begin{aligned} \alpha_\text{IR}(\omega) &\propto \omega^2 \int_{-\infty}^{+\infty} e^{-i\omega t} \langle \vec{\mu}(t)\vec{\mu}(0) \rangle \, \mathrm{d}t \\ &\propto \int_{-\infty}^{+\infty} e^{-i\omega t} \langle \dot{\vec{\mu}}(t)\dot{\vec{\mu}}(0) \rangle \, \mathrm{d}t \end{aligned} \tag{2}$$

The Raman scattering cross section $\sigma_\text{Raman}(\nu)$ as a function of the Raman frequency

shift ν is determined by the molecular polarizability tensor $\hat{p}$. Adding the parallel and perpendicular scattering contributions, the total cross section is given by[58,59]

$$\begin{aligned}\sigma_{\mathrm{Raman}}(\nu) &\propto \nu^4 \int_{-\infty}^{+\infty} e^{-i\nu t} \left[\langle p_{\mathrm{iso}}(t) p_{\mathrm{iso}}(0)\rangle + \frac{7}{30}\langle \mathrm{Tr}\hat{p}_{\mathrm{aniso}}(t)\hat{p}_{\mathrm{aniso}}(0)\rangle\right] \mathrm{d}t \\ &\propto \int_{-\infty}^{+\infty} e^{-i\nu t} \left[\langle \ddot{p}_{\mathrm{iso}}(t) \ddot{p}_{\mathrm{iso}}(0)\rangle + \frac{7}{30}\langle \mathrm{Tr}\ddot{\hat{p}}_{\mathrm{aniso}}(t)\ddot{\hat{p}}_{\mathrm{aniso}}(0)\rangle\right] \mathrm{d}t \end{aligned} \tag{3}$$

where $p_{\mathrm{iso}} = (1/3)\mathrm{Tr}\hat{p}$ and $\hat{p}_{\mathrm{aniso}} = \hat{p} - p_{\mathrm{iso}}\mathbb{1}$, with the 3×3 identity matrix $\mathbb{1}$, are the isotropic (scalar) and anisotropic (tensor) parts of the molecular polarizability. As suggested by Aida et al.,[58] the ν^4 factor was used to introduce the autocorrelation functions of the respective second time derivatives.

It is necessary to average the correlation functions of a number of independent MD runs in order to obtain reliable spectra.[59,60] We therefore used at least 50 different configurations of the single G4 molecule as starting structures, which were sampled from a 1 ns NVT trajectory of liquid G4 at $T = 298.15\,\mathrm{K}$. For each starting configuration, the NVT trajectory of the G4 molecule at $T = 298.15\,\mathrm{K}$ was propagated for 200 ps using the same time step, integrator, and thermostat as before. The total dipole moment $\vec{\mu}$ and polarizability tensor $\hat{p}$ of the G4 molecule was sampled every 0.5 fs. The respective first and second time derivatives were computed from finite differences and the autocorrelation functions $\langle\dot{\vec{\mu}}(t)\dot{\vec{\mu}}(0)\rangle$, $\langle\ddot{p}_{\mathrm{iso}}(t)\ddot{p}_{\mathrm{iso}}(0)\rangle$, and $\langle\mathrm{Tr}\ddot{\hat{p}}_{\mathrm{aniso}}(t)\ddot{\hat{p}}_{\mathrm{aniso}}(0)\rangle$ were then obtained by first performing a "sliding-window" average for each individual trajectory with 1000 different starting points $t = 0$ of the autocorrelation functions, taking the average of the forward and backward time direction, and then averaging all autocorrelation functions of the 50 independent MD runs with different initial G4 configurations. The autocorrelation functions were computed for 20000 time steps of 0.5 fs, corresponding to a total (positive) time span of 10 ps used for the Fourier transformations.

Spectroscopy experiments. Experimental Raman and IR spectra of tetraglyme (G4) were measured as a benchmark for the calculated spectra. Raman scattering was measured

at the 785 nm excitation line of a laser diode using a Renishaw Invia spectrometer equipped with a Peltier cooled CCD. Measurements were carried out in a micro-Raman configuration ($\times$50 objective lens) using a lab-made stainless-steel cell allowing controlled temperature (23 $^{\mathrm{deg}}$C) and atmospheric pressure of Ar gas. The measurements were performed through a non-interacting glass and samples were placed in a platinum crucible.

IR absorption spectra were recorded in attenuated total reflection (ATR) configuration using a Perkin Elmer spectrometer. The liquid samples were pressed between two KBr windows in a demountable OMNI-CELL transmission cell, prepared in an Ar-filled glove box with O_2 content below 1 ppm. The average of 32 scans in the range 500–4000 cm^{-1} was taken at a resolution of 1 cm^{-1}.

G4–cation complexation with AMOEBA. To assess battery-relevant electrolyte properties with the AMOEBA models, the complexation energies of alkali and alkaline-earth metal ions (Li^+, Na^+, K^+, Mg^{2+}, Ca^{2+}) with single G4 molecules were calculated. For comparison, complexation energies were also computed at the DFT PBE0-D4 level with a def2-TZVP basis set using the ORCA software package.[51] The G4–cation complex structures were optimized at the DFT level and the respective atomic coordinates are given in the SI. We compared three different levels of complexation energies according to the reaction M^{n+} + G4 $\rightarrow$ $[M(G4)]^{n+}$. First, the free G4 molecule (left-hand side of the reaction) was frozen in its structure of the DFT-relaxed G4–cation complexes. Second, the free G4 molecule was considered in the DFT-optimized minimum-energy structure of single G4 (linear configuration in Figure 1). Third, the structures of G4–cation complexes and free G4 molecules (linear configuration) were independently optimized both at the DFT level and with the AMOEBA models, the latter using the MINIMIZE tool of the Tinker software package.[43] We further used the DFT PBE0-D4 electronic density matrices for an NBO analysis (natural bond orbitals) of the $[M(G4)]^{n+}$ complexes with the NBO 7.0 program.[61]

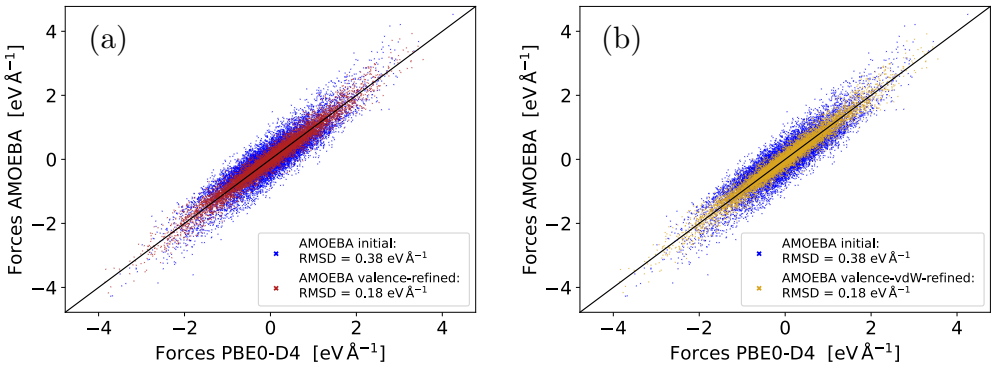

Figure 3: AMOEBA vs. PBE0-D4 forces for (a) the valence-refined (red) and (b) the valence-vdW-refined (gold) AMOEBA models, both in comparison to the initial, non-refined AMOEBA model (blue).

Results and Discussion

AMOEBA parameter refinement. As described in the Methods section, we tested a refinement procedure of the AMOEBA valence and vdW parameters for G4 based on fitting the atomic forces obtained from the AMOEBA model to *ab initio* forces computed at the PBE0-D4 level. A plot of the AMOEBA vs. PBE0-D4 forces is presented in Figure 3 for the valence-refined (a) and valence-vdW-refined (b) AMOEBA models, both in comparison to the initial, non-refined AMOEBA model. In both cases, the refined AMOEBA parametrization provided a significantly improved agreement with PBE0-D4 forces with a small root-mean-square deviation (RMSD) of 0.18 eV Å^{-1}. In contrast, the RMSD of the initial AMOEBA model was more than twice as large with a value of 0.38 eV Å^{-1}. However, no relevant difference was established between the valence-refined and valence-vdW-refined AMOEBA models based on the forces from the MD trajectory of a single G4 molecule. This is not surprising, because the only difference between these two flavors lies in the inclusion of the vdW parameters in the set of fitted parameters for the valence-vdW-refined model. Whereas van der Waals interactions are highly relevant for the description of intermolecular forces, the intramolecular interactions of a single G4 molecule are dominated by the valence part of the AMOEBA force field.

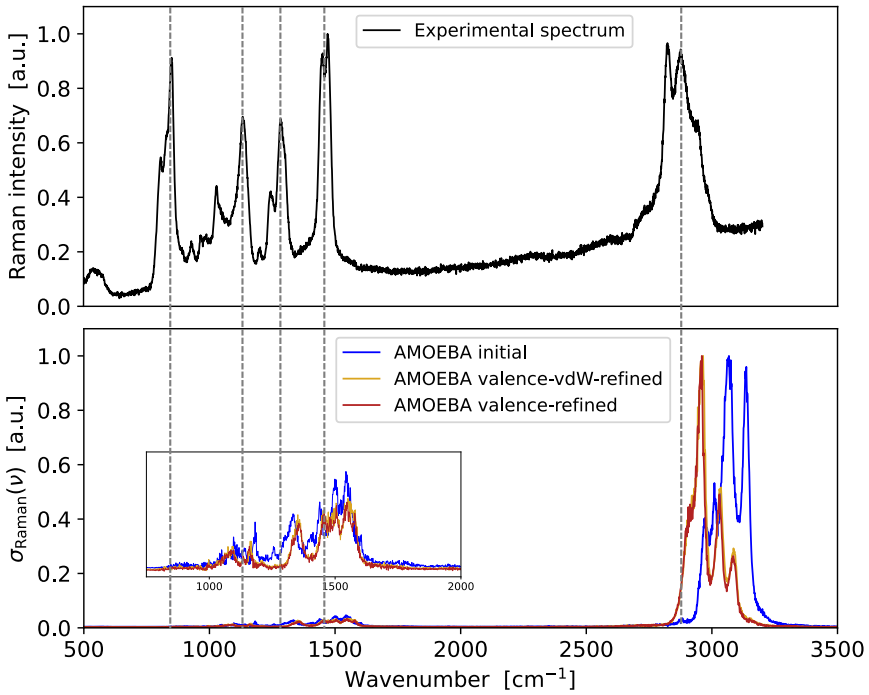

Figure 4: Raman spectra of tetraglyme (G4) computed with different flavors of the AMOEBA model (lower panel) in comparison to the experimental Raman spectrum (top panel). The inset in the lower panel shows an enlargement (×8) of the low-frequency spectral range on an aligned x-axis.

Raman and IR spectroscopy. Spectroscopic techniques provide insight into the atom-scale vibrational dynamics in the liquid. Within a harmonic approximation, the vibrational frequencies are proportional to the square root of the effective force constants, which, in turn, are the spatial derivatives of the atomic forces. We therefore consider the spectra useful probes for the quality of the description of atomic forces, and thus the local properties of the solvent, by the different flavors of the AMOEBA model and the parameter refinement strategy based on force-force fitting. Figure 4 shows a comparison of Raman spectra of tetraglyme (G4) computed from AMOEBA MD simulations with an experimentally measured spectrum (see SI Figure S1 for separately plotted spectra). The low-frequency range appears suppressed in the computed spectra which we attribute to the ν^4 factor contained in Eq. (3) resulting in a certain overemphasis of the high-frequency region. The inset in the lower panel of Figure 4 therefore presents an enlargement of the low-frequency range.

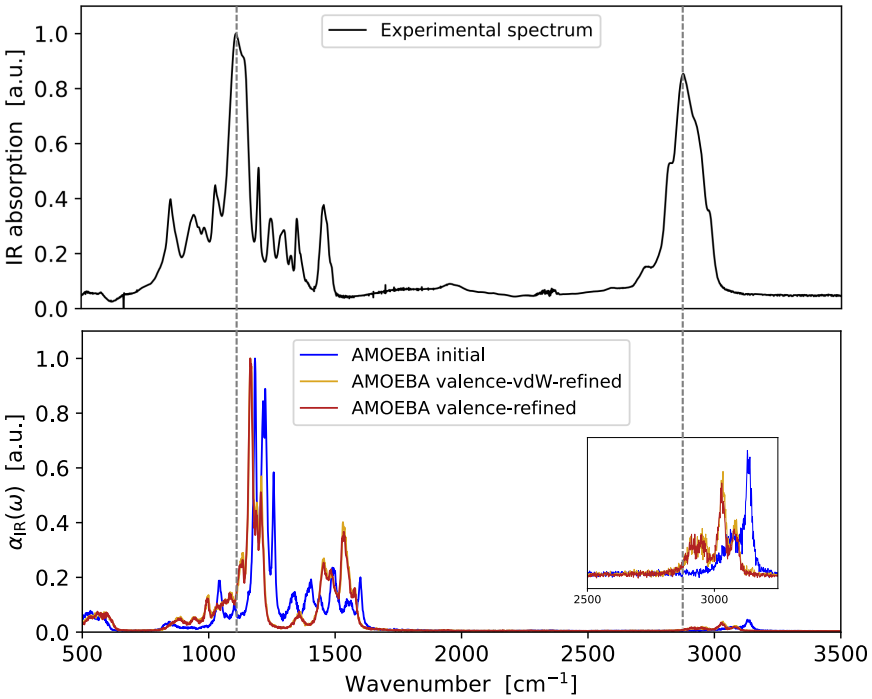

Figure 5: Infrared (IR) absorption spectra of tetraglyme (G4) computed with different flavors of the AMOEBA model (lower panel) in comparison to the experimental IR absorption spectrum (top panel). The inset in the lower panel shows an enlargement (×11) of the high-frequency spectral range on an aligned x-axis.

All relevant features of the spectrum are blue-shifted in the simulated spectra as compared to experiment. However, the dominant high-frequency peak around 3000 cm^{-1} of both the valence-refined and valence-vdW-refined AMOEBA models is red-shifted with respect to the one of the initial model and closer to the experimental peak. Also the triplet structure of the computed peak from the refined models fits well to the structure of the experimental high-frequency peak. The valence parameter refinement thus results in an improved description of the atomic scale dynamical properties of the glyme molecule by the AMOEBA force field. We note that the difference between the spectra of the valence-refined and valence-vdW-refined models is negligible, which agrees with the force-force fitting results discussed in the previous section. The inclusion of vdW parameters in the fitting procedure thus appears unnecessary from the perspective of atom-scale dynamical properties of single glyme molecules. Their effect on the macroscopic properties of the glyme liquid will be analyzed

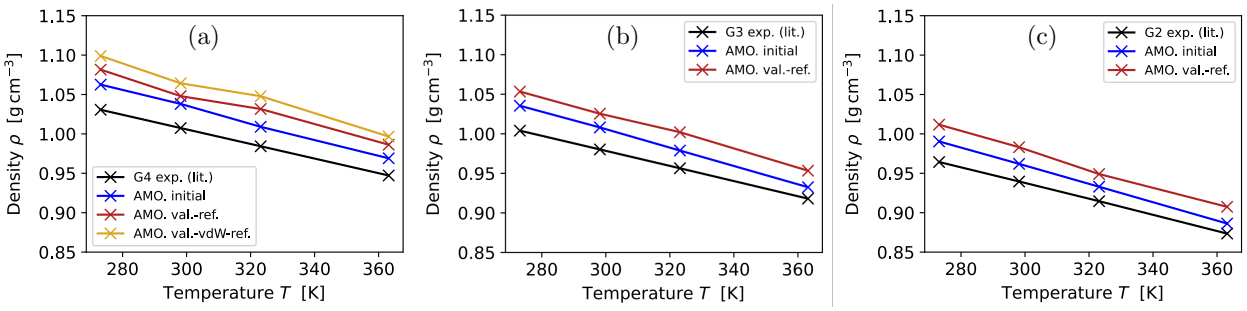

Figure 6: Liquid density ρ of (a) tetraglyme (G4), (b) triglyme (G3), and (c) diglyme (G2) at different temperatures and a pressure of $p = 1\,\mathrm{atm}$ obtained from AMOEBA MD simulations in comparison to experimental literature data.[62]

later.

A similar picture holds for the IR absorption spectra presented in Figure 5 (see SI Figure S2 for separately plotted spectra), where the lower frequency range appears overemphasized. Still, the same shifts of the high-frequency peak around $3000\,\mathrm{cm}^{-1}$ that were observed for the Raman spectra are also found in the IR spectra (see enlarged high-frequency region in the inset of the lower panel in Figure 5). In the low-frequency range, a similar situation is observed. The dominant absorption peak around 1100–$1200\,\mathrm{cm}^{-1}$ is blue shifted in the simulated spectra, but the valence-refined and valence-vdW-refined AMOEBA models perform better than the initial, non-refined model.

Table 1: Density ρ in $\mathrm{g\,cm}^{-3}$ of liquid tetraglyme (G4) at different temperatures and a pressure of $p = 1\,\mathrm{atm}$ obtained from MD simulations with the initial, valence-refined (val.-ref.), and valence-vdW-refined (val.-vdW-ref.) AMOEBA (AMO.) models, in comparison to experimental literature data.[62]

Temperature	Experiment[62]	AMO. initial	AMO. val.-ref.	AMO. val.-vdW-ref.
273.15 K	1.031	1.063	1.082	1.099
298.15 K	1.007	1.038	1.048	1.064
323.15 K	0.984	1.009	1.032	1.048
363.15 K	0.947	0.969	0.986	0.997

Density and dielectric constant of liquid glyme solvent. The simulated values of the liquid tetraglyme density at different temperatures and a pressure of $p = 1\,\mathrm{atm}$ are

compiled in Table 1 and plotted in Figure 6a. Experimental literature data[62] is shown for comparison. The decrease of the density with increasing temperature is well reproduced by the simulation results. However, the different AMOEBA models perform differently well when compared with the experimental data. Surprisingly, we find that the initial, non-refined model yields the best agreement with experiment with a slight overestimation of the density by approx. 3%, whereas the valence-refined and valence-vdW-refined models provide an overestimation by approx. 4–5% and 6%, respectively. As expected, the difference between the two refined models demonstrates that the liquid density is highly sensitive to small changes in the vdW parameters, cf. respective AMOEBA parametrizations in the SI. We find that the refinement of the vdW parameters on the basis of the force-force fitting procedure results in a worsened description of the liquid density. This is not surprising, because our procedure involves forces sampled from an MD trajectory of a single glyme molecule, and therefore does not include information about intermolecular forces between different glyme molecules that are relevant for the van der Waals part of the model. The intramolecular forces, in turn, are dominated by the valence parameters. When including the vdW parameters into the fitting of intramolecular forces, the vdW part tries to compensate for some of the errors of the valence part. This produces a biased set of vdW parameters with a deteriorated description of intermolecular interactions that determine the macroscopic liquid properties, such as the density. We therefore excluded the valence-vdW-refined model in the subsequent investigation of other glyme solvents. Figure 6b,c shows the simulated densities of triglyme (G3) and diglyme (G2) at different temperatures and a pressure of $p = 1\,\mathrm{atm}$. In both cases, the temperature-dependence of the density is well reproduced and the differences between simulation and experiment are very similar to the situation for G4. Importantly, the decreasing trend in the density as a function of decreasing glyme chain length is well described by the simulation results. This shows that the AMOEBA models developed for G4 are indeed transferable to the simulation of other glymes, supporting the validity of our universalization approach for the atomic monopole charges as described in

Table 2: Dielectric constant ϵ_r of liquid tetraglyme (G4) at $T = 298.15\,\mathrm{K}$ obtained from AMOEBA MD simulations in comparison to experimental literature data.[13]

Model	ϵ_r
Experiment[13]	7.78
AMOEBA initial	7.9 ± 0.1
AMOEBA valence-refined	9.0 ± 0.2
AMOEBA valence-vdW-refined	10.9 ± 0.2

the Methods section.

Table 2 presents the dielectric constant ϵ_r of liquid tetraglyme (G4) at $T = 298.15\,\mathrm{K}$ simulated with the different AMOEBA models in comparison to the experimental literature value of $\epsilon_r = 7.78$.[13] A similar trend is found as for the density. The initial, non-refined AMOEBA model yields $\epsilon_r = 7.9$ in excellent agreement with experiment. The valence-refined and valence-vdW-refined models overestimate the dielectric constant by 16% and 40%, respectively. Thus, whereas the valence-refined model still provides an acceptable agreement with experiment, the valence-vdW-refined model must be discarded based on the present results.

We conclude that both the initial and the valence-refined AMOEBA models well describe the macroscopic properties of glyme solvent in terms of density and dielectric constant. However, the non-refined model appears to slightly outperform the valence-refined one, which is certainly unexpected and opposite to our findings for the description of the spectroscopic properties. One possible explanation for this contradictory behavior could be errors in the DFT-derived forces that were used as reference data for the parameter refinement. However, the improved description of the spectroscopic properties with the refined AMOEBA model indicates an improved description of atomic forces, supporting the reliability of the DFT reference forces. Another possible explanation might be the neglect of nuclear quantum effects (NQEs) in classical MD simulations. In a recent study, Mauger et al.[63] demonstrated that including nuclear quantum effects in AMOEBA MD simulations *via* the adaptive quantum thermal bath method[64] resulted in an improved description of both thermodynamic

and spectroscopic properties of liquid water. The vibrational zero-point energy (ZPE) is a major manifestation of NQEs, which can be simulated by a frequency-dependent increased effective temperature during classical MD simulations. From Figure 6a, we observe that an increase in effective temperature by 20–50 K, depending on the model flavor, would decrease the simulated density values down to the experimental one. We therefore consider NQEs a likely source of the observed discrepancies in the density and dielectric constant obtained from AMOEBA models in comparison to experiment. To further test this hypothesis, we simulated the dielectric constant with the valence-vdW-refined model at a 50 K-increased temperature of $T = 348.15\,\mathrm{K}$ and obtained a value of $\epsilon_r = 8.9 \pm 0.1$, which agrees significantly better with the experimental value at $T = 298.15\,\mathrm{K}$ than the computed value for this model at $T = 298.15\,\mathrm{K}$, see Table 2. We consider this a proof of concept that including NQEs will be relevant for a concluding assessment of our AMOEBA models. As soon as the respective implementation in Tinker-HP will be released, we therefore envisage to re-evaluate the AMOEBA models including NQEs.

G4–cation complexation. The complexation energies $\Delta E_{\mathrm{cpx}} = E_{\mathrm{G4–cation}} - E_{\mathrm{G4}} - E_{\mathrm{cation}}$ of various alkali and alkaline-earth metal ions with single G4 molecules are shown in Figure 7. The results from the initial and valence-refined AMOEBA models are compared with DFT PBE0-D4 results. The complexation energies in Figure 7a were obtained with a frozen G4 configuration in the free state as within the complex. As a result, all contributions of the AMOEBA valence parameters get cancelled in the corresponding complexation energy, and ΔE_{cpx} only depends on the vdW and electrostatic interactions between G4 and cations. Accordingly, the results for both the initial and valence-refined AMOEBA models, which only differ in the valence part, are identical. In contrast, different structures of G4 in the free state as compared to the complex were considered in Figure 7b,c. This makes the resulting complexation energies slightly dependent on the AMOEBA valence parameters, but the influence of the vdW and electrostatic interactions is clearly dominating, as shown

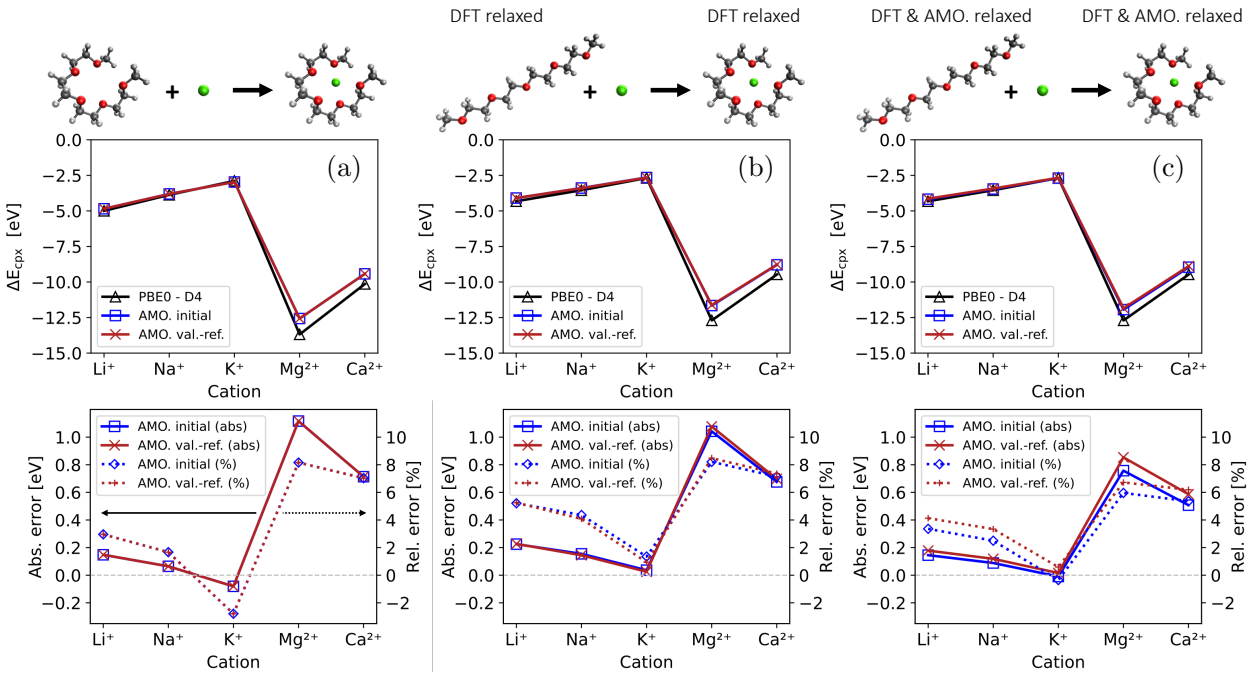

Figure 7: Complexation energies ΔE_{cpx} of various alkali and alkaline-earth metal ions with single G4 molecules calculated with the initial and valence-refined (val.-ref.) AMOEBA models in comparison to DFT PBE0-D4 results (top panels). The corresponding absolute and relative errors of the AMOEBA results with respect to DFT PBE0-D4 are shown in the bottom panels. Complexation energies are shown for the frozen G4 structure (a), the DFT-relaxed minimum-energy structures (b), and the independently relaxed structures with AMOEBA and DFT (c). The respective reactions $\mathrm{G4}+\mathrm{M}^{n+} \rightarrow [\mathrm{M(G4)}]^{n+}$ are schematically shown above.

by the similarity with the results in Figure 7a. Therefore, no relevant difference is observed between the initial and valence-refined AMOEBA models. We note that the best agreement between AMOEBA and DFT results was obtained when the structures of the involved species were independently relaxed at the AMOEBA and DFT levels, see Figure 7c. The structural relaxation thus provided a slight compensation of errors.

In general, we find an excellent agreement between the complexation energies from AMOEBA and DFT PBE0-D4 for the monovalent alkali metal ions Li^+, Na^+, and K^+ with absolute errors less than 0.2 eV, corresponding to relative errors less than 5%. The absolute value of the complexation energy decreases with increasing size of the alkali metal ion, as could be expected from the weaker electrostatic interactions at increased distance between the cation center and the coordinating EO atoms of the G4 ligand. It is interesting

Table 3: Results from natural bond orbital (NBO) analysis for $[M(G4)]^{n+}$ complexes with different mono- and divalent cations M^{n+}. The natural charge Q and the occupancy of the valence s-type NBO of the cation are given.

Cation	Q / e	s-orbital occupancy / e^-
Li^+	0.899	0.092
Na^+	0.920	0.072
K^+	0.947	0.042
Mg^{2+}	1.825	0.151
Ca^{2+}	1.850	0.073

to note that the AMOEBA models correctly reproduce this trend, as shown by the results for independently relaxed structures in Figure 7c. We highlight that, at this stage, the complexation energies of the potassium ion obtained from the AMOEBA models are essentially identical to the DFT PBE0-D4 result, and the relative errors for the sodium and lithium ions are about 3–4%, only. The AMOEBA models thus provide almost *ab initio* precision for the description of the interactions between alkali metal ions and glyme solvent. This is very promising for future electrolyte MD simulations with the developed AMOEBA models.

For the divalent alkaline-earth metal ions Mg^{2+} and Ca^{2+}, the agreement between AMOEBA and DFT results is significantly reduced as compared to the monovalent ions, with absolute errors between 0.6–1.1 eV, corresponding to relative errors of 6–8%. The strongly increased relative errors demonstrate a disproportionate error enhancement that cannot be explained on the basis of the double charge of the divalent ions alone. We consider partial electron transfer from the glyme ligand EOs to the alkaline-earth metal cation as a likely reason for the decreased quality of the AMOEBA-derived complexation energies. This is confirmed by an NBO analysis[61] of the $[M(G4)]^{n+}$ complexes. The results shown in Table 3 demonstrate the more important electron transfer to the (formally vacant) valence s orbital of the metal for the case of the divalent alkaline-earth metal ions in comparison to the corresponding monovalent alkali metal ions of the same row (compare Na^+ to Mg^{2+} and K^+ to Ca^{2+}). Clearly, the fixed integer charges of the metal ions within the AMOEBA model oppose such a picture of charge repartitioning in $[M(G4)]^{n+}$ complexes. For non-polarizable

force fields this shortcoming has been mitigated by charge rescaling.[26] For polarizable force fields, such as AMOEBA, the atomic polarizabilities inherently enable to mimic the charge repartitioning as a function of the local environment. Still, it is not surprising that a highly accurate description of the interaction between alkaline-earth metal ions and glyme EOs remains challenging for the AMOEBA force field. However, along an MD trajectory, we expect the cation–EO bonds to be formed, or broken, one after the other, so that only errors *per cation–EO bond* matter. Taking into account that the cations of the investigated complexes are coordinated by five ether oxygen atoms, the absolute errors per cation–EO bond are about 0.1–0.2 eV, only. We therefore consider the AMOEBA models to be sufficiently accurate also for the simulation of glyme-based electrolytes comprising alkaline-earth metal ions.

Conclusion

We constructed AMOEBA models for the glyme solvent family. To this end, the charge monopole parameters determined for tetraglyme were universalized to yield charge-neutral building blocks of the glyme molecule that can be connected to form charge-neutral glymes of various lengths. Three different flavors of the AMOEBA model were developed. Two of them included the refinement of non-electrostatic parameters based on force-force fitting with DFT-derived forces as a reference. The refinement of valence parameters resulted in an improved description of the atom-scale dynamical properties, which was shown by the comparison of simulated and experimental Raman and IR spectra. The macroscopic thermodynamic properties of the glyme liquids, however, namely the density and dielectric constant, were better simulated with the non-refined model. In particular, including also van der Waals parameters in the refinement procedure resulted in a rather poor agreement with experimental literature values. Overall, the (only) valence-refined AMOEBA model provided a good compromise between an accurate description of spectroscopic properties, as well as

liquid glyme density and dielectric constant. We expect that accounting for nuclear quantum effects in future AMOEBA MD simulations will further improve the agreement between model results and experiment. The developed AMOEBA models yielded complexation energies between alkali/alkaline-earth metal cations and single tetraglyme molecules that were in good agreement with quantum-based results at the DFT PBE0-D4 level. We thus consider the developed AMOEBA models suitable for reliable MD simulations of glyme-based battery electrolytes to be performed in subsequent works. Moreover, the universalization and refinement procedure of AMOEBA parameters can be useful for the construction of AMOEBA models for other battery electrolytes, in particular polymer electrolyte systems.

Acknowledgement

This work was supported by the European FET-Open project VIDICAT (Grant Agreement: 829145). Nicolas Sergent and Cristina Iojoiu are acknowledged for their support in spectroscopy experiments.

Supporting Information Available

Coordinate files of G4 configurations and G4–cation complexes; Parameter files of AMOEBA models for glyme solvents incl. cations. This material is available free of charge via the Internet at `http://pubs.acs.org/`.

References

(1) Xu, K. Electrolytes and Interphases in Li-Ion Batteries and Beyond. *Chem. Rev.* **2014**, *114*, 11503–11618.

(2) Di Lecce, D.; Marangon, V.; Jung, H.-G.; Tominaga, Y.; Greenbaum, S.; Hassoun, J.

Glyme-based electrolytes: suitable solutions for next-generation lithium batteries. *Green Chem.* **2022**, *24*, 1021–1048.

(3) Aurbach, D.; Granot, E. The study of electrolyte solutions based on solvents from the "glyme" family (linear polyethers) for secondary Li battery systems. *Electrochimica Acta* **1997**, *42*, 697–718.

(4) Brouillette, D.; Perron, G.; Desnoyers, J. E. Apparent Molar Volume, Heat Capacity, and Conductance of Lithium Bis(trifluoromethylsulfone)imide in Glymes and Other Aprotic Solvents. *Journal of Solution Chemistry* **1998**, *27*, 151–182.

(5) Brouillette, D.; Irish, D. E.; Taylor, N. J.; Perron, G.; Odziemkowski, M.; Desnoyers, J. E. Stable solvates in solution of lithium bis(trifluoromethylsulfone)imide in glymes and other aprotic solvents: Phase diagrams, crystallography and Raman spectroscopy. *Phys. Chem. Chem. Phys.* **2002**, *4*, 6063–6071.

(6) Hayamizu, K. Direct relations between ion diffusion constants and ionic conductivity for lithium electrolyte solutions. *Electrochimica Acta* **2017**, *254*, 101–111.

(7) Henderson, W. A. Glyme–Lithium Salt Phase Behavior. *The Journal of Physical Chemistry B* **2006**, *110*, 13177–13183.

(8) Tamura, T.; Hachida, T.; Yoshida, K.; Tachikawa, N.; Dokko, K.; Watanabe, M. New glyme–cyclic imide lithium salt complexes as thermally stable electrolytes for lithium batteries. *Journal of Power Sources* **2010**, *195*, 6095–6100.

(9) Saito, M.; Yamada, S.; Ishikawa, T.; Otsuka, H.; Ito, K.; Kubo, Y. Factors influencing fast ion transport in glyme-based electrolytes for rechargeable lithium–air batteries. *RSC Adv.* **2017**, *7*, 49031–49040.

(10) Yamijala, S. S. R. K. C.; Kwon, H.; Guo, J.; Wong, B. M. Stability of Calcium Ion

Battery Electrolytes: Predictions from Ab Initio Molecular Dynamics Simulations. *ACS Applied Materials & Interfaces* **2021**, *13*, 13114–13122.

(11) Maroni, F.; Dongmo, S.; Gauckler, C.; Marinaro, M.; Wohlfahrt-Mehrens, M. Through the Maze of Multivalent-Ion Batteries: A Critical Review on the Status of the Research on Cathode Materials for Mg^{2+} and Ca^{2+} Ions Insertion. *Batteries & Supercaps* **2021**, *4*, 1221–1251.

(12) Pagot, G.; Vezzù, K.; Martinez-Cisneros, C. S.; Antonelli, C.; Levenfeld, B.; Varez, A.; Sanchez, J.-Y.; Di Noto, V. Interplay between Conductivity, Matrix Relaxations and Composition of Ca-Polyoxyethylene Polymer Electrolytes. *ChemElectroChem* **2021**, *8*, 2459–2466.

(13) Riadigos, C.; Iglesias, R.; Rivas, M.; Iglesias, T. Permittivity and density of the systems (monoglyme, diglyme, triglyme, or tetraglyme+n-heptane) at several temperatures. *J. Chem. Thermodynamics* **2011**, *43*, 275–283.

(14) Payne, V. A.; Xu, J.-h.; Forsyth, M.; Ratner, M. A.; Shriver, D. F.; de Leeuw, S. W. Molecular dynamics simulations of ion clustering and conductivity in NaI/ether solutions. II. Effect of ion concentration. *The Journal of Chemical Physics* **1995**, *103*, 8746–8755.

(15) Henderson, W. A.; McKenna, F.; Khan, M. A.; Brooks, N. R.; Young, V. G.; Frech, R. Glyme–Lithium Bis(trifluoromethanesulfonyl)imide and Glyme–Lithium Bis(perfluoroethanesulfonyl)imide Phase Behavior and Solvate Structures. *Chemistry of Materials* **2005**, *17*, 2284–2289.

(16) Jankowski, P.; Dranka, M.; Wieczorek, W.; Johansson, P. TFSI and TDI Anions: Probes for Solvate Ionic Liquid and Disproportionation-Based Lithium Battery Electrolytes. *The Journal of Physical Chemistry Letters* **2017**, *8*, 3678–3682.

(17) Nguyen, L. H. B.; Picard, T.; Sergent, N.; Raynaud, C.; Filhol, J.-S.; Doublet, M.-L. Investigation of alkali and alkaline earth solvation structures in tetraglyme solvent. *Phys. Chem. Chem. Phys.* **2021**, *23*, 26120–26129.

(18) Pappenfus, T. M.; Henderson, W. A.; Owens, B. B.; Mann, K. R.; Smyrl, W. H. Complexes of Lithium Imide Salts with Tetraglyme and Their Polyelectrolyte Composite Materials. *Journal of The Electrochemical Society* **2004**, *151*, A209–A215.

(19) Austen Angell, C.; Ansari, Y.; Zhao, Z. Ionic Liquids: Past, present and future. *Faraday Discuss.* **2012**, *154*, 9–27.

(20) Mandai, T.; Yoshida, K.; Ueno, K.; Dokko, K.; Watanabe, M. Criteria for solvate ionic liquids. *Phys. Chem. Chem. Phys.* **2014**, *16*, 8761–8772.

(21) Nguyen, L. H. B.; Picard, T.; Iojoiu, C.; Alloin, F.; Sergent, N.; Doublet, M.-L.; Filhol, J.-S. Investigating the abnormal conductivity behaviour of divalent cations in low dielectric constant tetraglyme-based electrolytes. *Phys. Chem. Chem. Phys.* **2022**, –.

(22) Bedrov, D.; Piquemal, J.-P.; Borodin, O.; MacKerell, A. D.; Roux, B.; Schröder, C. Molecular Dynamics Simulations of Ionic Liquids and Electrolytes Using Polarizable Force Fields. *Chemical Reviews* **2019**, *119*, 7940–7995.

(23) Payne, V. A.; Xu, J.-h.; Forsyth, M.; Ratner, M. A.; Shriver, D. F.; de Leeuw, S. W. Molecular dynamics simulations of ion clustering and conductivity in NaI/ether solutions. I. Effect of ion charge. *The Journal of Chemical Physics* **1995**, *103*, 8734–8745.

(24) Lapidus, S. H.; Rajput, N. N.; Qu, X.; Chapman, K. W.; Persson, K. A.; Chupas, P. J. Solvation structure and energetics of electrolytes for multivalent energy storage. *Phys. Chem. Chem. Phys.* **2014**, *16*, 21941–21945.

(25) Rajput, N. N.; Qu, X.; Sa, N.; Burrell, A. K.; Persson, K. A. The Coupling between Stability and Ion Pair Formation in Magnesium Electrolytes from First-Principles Quan-

tum Mechanics and Classical Molecular Dynamics. *Journal of the American Chemical Society* **2015**, *137*, 3411–3420.

(26) Costa, L. T.; Sun, B.; Jeschull, F.; Brandell, D. Polymer-ionic liquid ternary systems for Li-battery electrolytes: Molecular dynamics studies of LiTFSI in a EMIm-TFSI and PEO blend. *The Journal of Chemical Physics* **2015**, *143*, 024904.

(27) Molinari, N.; Mailoa, J. P.; Kozinsky, B. Effect of Salt Concentration on Ion Clustering and Transport in Polymer Solid Electrolytes: A Molecular Dynamics Study of PEO–LiTFSI. *Chemistry of Materials* **2018**, *30*, 6298–6306.

(28) Borodin, O.; Smith, G. D. Development of Many-Body Polarizable Force Fields for Li-Battery Components: 1. Ether, Alkane, and Carbonate-Based Solvents. *The Journal of Physical Chemistry B* **2006**, *110*, 6279–6292.

(29) Borodin, O.; Smith, G. D. Development of Many-Body Polarizable Force Fields for Li-Battery Applications: 2. LiTFSI-Doped Oligoether, Polyether, and Carbonate-Based Electrolytes. *The Journal of Physical Chemistry B* **2006**, *110*, 6293–6299.

(30) Eilmes, A.; Kubisiak, P. Li^+–Oligoglyme Association in the Presence of Ionic Liquid Studied by Molecular Dynamics and Explicit or Implicit Solvent Model. *The Journal of Physical Chemistry B* **2015**, *119*, 11708–11720.

(31) Dong, D.; Bedrov, D. Charge Transport in [Li(tetraglyme)][bis(trifluoromethane) sulfonimide] Solvate Ionic Liquids: Insight from Molecular Dynamics Simulations. *The Journal of Physical Chemistry B* **2018**, *122*, 9994–10004.

(32) Liyana-Arachchi, T. P.; Haskins, J. B.; Burke, C. M.; Diederichsen, K. M.; McCloskey, B. D.; Lawson, J. W. Polarizable Molecular Dynamics and Experiments of 1,2-Dimethoxyethane Electrolytes with Lithium and Sodium Salts: Structure and Transport Properties. *The Journal of Physical Chemistry B* **2018**, *122*, 8548–8559.

(33) Kubisiak, P.; Eilmes, A. Solvation of Mg^{2+} Ions in $Mg(TFSI)_2$–Dimethoxyethane Electrolytes—A View from Molecular Dynamics Simulations. *The Journal of Physical Chemistry C* **2018**, *122*, 12615–12622.

(34) Wróbel, P.; Kubisiak, P.; Eilmes, A. NaFSI and NaTFSI Solutions in Ether Solvents from Monoglyme to Poly(ethylene oxide)—A Molecular Dynamics Study. *The Journal of Physical Chemistry B* **2021**, *125*, 10293–10303.

(35) Yan, T.; Burnham, C. J.; Del Pópolo, M. G.; Voth, G. A. Molecular Dynamics Simulation of Ionic Liquids: The Effect of Electronic Polarizability. *The Journal of Physical Chemistry B* **2004**, *108*, 11877–11881.

(36) Borodin, O. Polarizable Force Field Development and Molecular Dynamics Simulations of Ionic Liquids. *The Journal of Physical Chemistry B* **2009**, *113*, 11463–11478.

(37) Ren, P.; Ponder, J. W. Polarizable Atomic Multipole Water Model for Molecular Mechanics Simulation. *The Journal of Physical Chemistry B* **2003**, *107*, 5933–5947.

(38) Starovoytov, O. N.; Torabifard, H.; Cisneros, G. A. Development of AMOEBA Force Field for 1,3-Dimethylimidazolium Based Ionic Liquids. *The Journal of Physical Chemistry B* **2014**, *118*, 7156–7166.

(39) Torabifard, H.; Reed, L.; Berry, M. T.; Hein, J. E.; Menke, E.; Cisneros, G. A. Computational and experimental characterization of a pyrrolidinium-based ionic liquid for electrolyte applications. *The Journal of Chemical Physics* **2017**, *147*, 161731.

(40) Klajmon, M.; Červinka, C. Does Explicit Polarizability Improve Simulations of Phase Behavior of Ionic Liquids? *Journal of Chemical Theory and Computation* **2021**, *17*, 6225–6239.

(41) Lagardère, L.; Jolly, L.-H.; Lipparini, F.; Aviat, F.; Stamm, B.; Jing, Z. F.; Harger, M.; Torabifard, H.; Cisneros, G. A.; Schnieders, M. J. et al. Tinker-HP: a massively parallel

molecular dynamics package for multiscale simulations of large complex systems with advanced point dipole polarizable force fields. *Chem. Sci.* **2018**, *9*, 956–972.

(42) Ponder, J. W.; Wu, C.; Ren, P.; Pande, V. S.; Chodera, J. D.; Schnieders, M. J.; Haque, I.; Mobley, D. L.; Lambrecht, D. S.; DiStasio, R. A. et al. Current Status of the AMOEBA Polarizable Force Field. *The Journal of Physical Chemistry B* **2010**, *114*, 2549–2564.

(43) Ren, P.; Wu, C.; Ponder, J. W. Polarizable Atomic Multipole-Based Molecular Mechanics for Organic Molecules. *Journal of Chemical Theory and Computation* **2011**, *7*, 3143–3161.

(44) Turney, J. M.; Simmonett, A. C.; Parrish, R. M.; Hohenstein, E. G.; Evangelista, F. A.; Fermann, J. T.; Mintz, B. J.; Burns, L. A.; Wilke, J. J.; Abrams, M. L. et al. Psi4: an open-source ab initio electronic structure program. *WIREs Computational Molecular Science* **2012**, *2*, 556–565.

(45) Feyereisen, M.; Fitzgerald, G.; Komornicki, A. Use of approximate integrals in ab initio theory. An application in MP2 energy calculations. *Chemical Physics Letters* **1993**, *208*, 359–363.

(46) Stone, A. J. Distributed Multipole Analysis: Stability for Large Basis Sets. *Journal of Chemical Theory and Computation* **2005**, *1*, 1128–1132.

(47) Virtanen, P.; Gommers, R.; Oliphant, T. E.; Haberland, M.; Reddy, T.; Cournapeau, D.; Burovski, E.; Peterson, P.; Weckesser, W.; Bright, J. et al. SciPy 1.0: Fundamental Algorithms for Scientific Computing in Python. *Nature Methods* **2020**, *17*, 261–272.

(48) Marcolongo, A.; Binninger, T.; Zipoli, F.; Laino, T. Simulating Diffusion Properties of Solid-State Electrolytes via a Neural Network Potential: Performance and Training Scheme. *ChemSystemsChem* **2020**, *2*, e1900031.

(49) Perdew, J. P.; Ernzerhof, M.; Burke, K. Rationale for mixing exact exchange with density functional approximations. *The Journal of Chemical Physics* **1996**, *105*, 9982–9985.

(50) Caldeweyher, E.; Ehlert, S.; Hansen, A.; Neugebauer, H.; Spicher, S.; Bannwarth, C.; Grimme, S. A generally applicable atomic-charge dependent London dispersion correction. *The Journal of Chemical Physics* **2019**, *150*, 154122.

(51) Neese, F.; Wennmohs, F.; Becker, U.; Riplinger, C. The ORCA quantum chemistry program package. *The Journal of Chemical Physics* **2020**, *152*, 224108.

(52) Martínez, L.; Andrade, R.; Birgin, E. G.; Martínez, J. M. PACKMOL: A package for building initial configurations for molecular dynamics simulations. *Journal of Computational Chemistry* **2009**, *30*, 2157–2164.

(53) Swope, W. C.; Andersen, H. C.; Berens, P. H.; Wilson, K. R. A computer simulation method for the calculation of equilibrium constants for the formation of physical clusters of molecules: Application to small water clusters. *The Journal of Chemical Physics* **1982**, *76*, 637–649.

(54) Bussi, G.; Donadio, D.; Parrinello, M. Canonical sampling through velocity rescaling. *The Journal of Chemical Physics* **2007**, *126*, 014101.

(55) Berendsen, H. J. C.; Postma, J. P. M.; van Gunsteren, W. F.; DiNola, A.; Haak, J. R. Molecular dynamics with coupling to an external bath. *The Journal of Chemical Physics* **1984**, *81*, 3684–3690.

(56) Neumann, M. Dipole moment fluctuation formulas in computer simulations of polar systems. *Molecular Physics* **1983**, *50*, 841–858.

(57) Jorge, M.; Lue, L. The dielectric constant: Reconciling simulation and experiment. *The Journal of Chemical Physics* **2019**, *150*, 084108.

(58) Aida, M.; Dupuis, M. IR and Raman intensities in vibrational spectra from direct ab initio molecular dynamics: D_2O as an illustration. *Journal of Molecular Structure: THEOCHEM* **2003**, *633*, 247–255.

(59) Fischer, S. A.; Ueltschi, T. W.; El-Khoury, P. Z.; Mifflin, A. L.; Hess, W. P.; Wang, H.-F.; Cramer, C. J.; Govind, N. Infrared and Raman Spectroscopy from Ab Initio Molecular Dynamics and Static Normal Mode Analysis: The C−H Region of DMSO as a Case Study. *The Journal of Physical Chemistry B* **2016**, *120*, 1429–1436.

(60) Horníček, J.; Kaprálová, P.; Bouř, P. Simulations of vibrational spectra from classical trajectories: Calibration with ab initio force fields. *The Journal of Chemical Physics* **2007**, *127*, 084502.

(61) Glendening, E. D.; Landis, C. R.; Weinhold, F. NBO 7.0: New vistas in localized and delocalized chemical bonding theory. *Journal of Computational Chemistry* **2019**, *40*, 2234–2241.

(62) Kodama, D.; Kanakubo, M.; Kokubo, M.; Hashimoto, S.; Nanjo, H.; Kato, M. Density, viscosity, and solubility of carbon dioxide in glymes. *Fluid Phase Equilibria* **2011**, *302*, 103–108.

(63) Mauger, N.; Plé, T.; Lagardère, L.; Huppert, S.; Piquemal, J.-P. Improving Condensed Phase Water Dynamics with Explicit Nuclear Quantum Effects: the Polarizable Q-AMOEBA Force Field. 2022; `https://arxiv.org/abs/2206.13430`.

(64) Mangaud, E.; Huppert, S.; Plé, T.; Depondt, P.; Bonella, S.; Finocchi, F. The Fluctuation–Dissipation Theorem as a Diagnosis and Cure for Zero-Point Energy Leakage in Quantum Thermal Bath Simulations. *Journal of Chemical Theory and Computation* **2019**, *15*, 2863–2880.